UNIVERSITY
OF TRENTO

DIPARTIMENTO DI INGEGNERIA E SCIENZA DELL'INFORMAZIONE

38123 Povo – Trento (Italy), Via Sommarive 14
http://www.disi.unitn.it

DEALING WITH MULTI-FREQUENCY SCATTERING DATA THROUGH THE IMSA

D. Franceschini, M. Donelli, R. Azaro, and A. Massa

January 2011

Technical Report # DISI-11-068

Dealing with Multi-Frequency Scattering Data through the IMSA

Davide Franceschini, Massimo Donelli, Renzo Azaro, and Andrea Massa

Department of Information and Communication Technology

University of Trento -Via Sommarive, 14 - 38050 Trento - ITALY

Tel.: +39 0461 882057; Fax: +39 0461 882093

E-mail: *andrea.massa@ing.unitn.it*,

{*davide.franceschini*, *massimo.donelli*, *renzo.azaro*}*@dit.unitn.it*

Web-site: *http://www.eledia.ing.unitn.it*

Dealing with Multi-Frequency Scattering Data through the IMSA

Davide Franceschini, Massimo Donelli, Renzo Azaro, and Andrea Massa

Abstract

This contribution presents a set of representative results obtained with two multi-resolution strategies developed for dealing with multi-frequency inverse scattering experiments starting from the iterative multi-scaling approach previously studied for monochromatic illuminations. The first approach is concerned with the integration of the iterative multi-scaling algorithm into a frequency-hopping reconstruction scheme, while the second one allows a multi-resolution simultaneous processing of multi-frequency data. The numerical and the experimental analysis are aimed at assessing both the reconstruction effectiveness and the required computational costs of the two- and three-dimensional implementations of the proposed inversion schemes in comparison with the monochromatic multi-step process and to the single-step optimization strategy, as well.

Key words:

Microwave Imaging, Electromagnetic Inverse Scattering, Multi-Frequency Data, Multi-Resolution Technique, Iterative Multi-Scaling Approach.

1 Introduction

Microwave imaging techniques are aimed at processing the scattered electromagnetic radiation collected in a non-invasive fashion on an external measurement region for determining the electromagnetic properties of an inaccessible area of investigation [1]-[3].

A key problem related to such techniques is the lack of collectable information on the scenario under test. As a matter of fact, the information content available from the scattering experiments cannot be arbitrarily increased by oversampling the scattered field [4] and, since single-illumination measurement setups do not usually allow a detailed reconstruction of unknown scatterers, multi-view and multi-illumination acquisition systems have been proposed [5] for increasing the amount of informative data. In such a context, several works have shown that frequency-hopping strategies (e.g., [6]) or the simultaneous processing of multi-frequency data [7]-[9] can improve the reconstruction capabilities of inverse scattering algorithms.

However, multi-frequency strategies have some intrinsic drawbacks to be carefully addressed for realizing effective and reliable inversion schemes. From the point of view of software/hardware resources, the increase of inversion data unavoidably needs of additional computational and storage resources with respect to monochromatic reconstruction methodologies. Moreover, the object function modeling the dielectric and conductivity parameters of the medium varies in relation to the working frequency and according to the dispersion model. Therefore, suitable countermeasures are commonly adopted, which consider a narrow range of frequencies or assume a Maxwellian model for describing the relationship between dielectric parameters and operating frequency (e.g., [7] and [8]).

On the other hand, even though possible advantages of using multi-frequency measures have been deeply investigated in the framework of single-step inversion algorithms, a limited literature deals with the exploitation of multi-frequency information through multi-resolution strategies [10]. Therefore, this paper is aimed at developing such an issue by investigating how a multi-frequency approach can be profitably integrated into a multi-step inversion algorithm ($IMSA$) [11][12] previously studied facing monochromatic data. This interest is mainly motivated from the non-negligible advantages that are expected. As a matter of fact, multi-frequency strategies based on the $IMSA$ could better ex-

ploit the well-known benefits of a multi-resolution expansion of the unknown space (e.g., [11]-[14]) taking into account the enlarged set of information coming from the scattering experiments at different frequencies.

The paper is organized as follows. The mathematical formulation of the multi-frequency approaches based on the $IMSA$ is briefly summarized in Sect. 2 as far as the two-dimensional case is concerned, while a set of representative synthetic as well as experimental results (regarding two- and three-dimensional configurations of dielectric and lossy bodies) are shown and discussed in Sect. 3. Finally, in Sect. 4, some conclusions and further possible developments will be outlined.

2 Mathematical Formulation

For simplicity, let us refer to a two-dimensional scenario (Fig. 1) characterized by an inhomogeneous cross section D_I lying in a homogeneous host medium (ε_0, μ_0) and illuminated by a set of P monochromatic (f_p being the working frequency of the p-th illumination, $p = 1, ..., P$) incident electric fields TM-polarized impinging from V different directions ($\mathbf{E}^{inc}_{v,p}(x,y) = E^{inc}_{v,p}(x,y)\hat{\mathbf{z}}$, $v = 1, ..., V$, $p = 1, ..., P$). The multi-frequency information available from the scattered radiation $\mathbf{E}^{tot}_{v,p}(x_{m_{v,p}}, y_{m_{v,p}}) = E^{tot}_{v,p}(x_{m_{v,p}}, y_{m_{v,p}})\hat{\mathbf{z}}$, collected at $m_{v,p} = 1, ..., M_{v,p}$ points belonging to the observation domain D_O, has to be efficiently exploited for reconstructing the frequency-dependent contrast function

$$\tau_p(x,y) = \varepsilon_r(x,y) - 1 - j\frac{\sigma(x,y)}{2\pi f_p \varepsilon_o} \qquad p = 1, ..., P \tag{1}$$

$\varepsilon_r(x,y)$ and $\sigma(x,y)$ being the relative permittivity and the conductivity, respectively. The characteristics of the scenario under test $\tau_p(x,y)$, $p = 1, ..., P$, are related to the scattering data (namely, the scattered field in the observation domain, $E^{scatt}_{v,p}(x,y)$, $(x,y) \in D_O$, and the incident field in the investigation domain, $E^{inc}_{v,p}(x,y)$, $(x,y) \in D_I$) through the Lippmann-Schwinger scattering equations [11]

$$E^{scatt}_{v,p}\left(x_{m_{v,p}}, y_{m_{v,p}}\right) = S^{ext}_{v,p}\left\{\tau_p(x,y)E^{tot}_{v,p}(x,y)\right\} \qquad \begin{array}{c}(x,y) \in D_I \\ \left(x_{m_{v,p}}, y_{m_{v,p}}\right) \in D_O\end{array} \tag{2}$$

$$E^{inc}_{v,p}(x,y) = E^{tot}_{v,p}(x,y) - S^{int}_{v,p}\left\{\tau_p(x,y)E^{tot}_{v,p}(x,y)\right\} \quad (x,y) \in D_I \tag{3}$$

where $S^{ext}_{v,p}$ and $S^{int}_{v,p}$ denote the external and internal scattering operator, respectively, and $E^{scatt}_{v,p}$ is defined as $E^{scatt}_{v,p}(x,y) = E^{tot}_{v,p}(x,y) - E^{inc}_{v,p}(x,y)$.

In order to effectively deal with multi-frequency data by solving (2) and (3) in terms of the unknown contrast function $\tau_p(x,y)$, $p = 1, ..., P$, two multi-resolution methodologies based on the $IMSA$ will be proposed in the following.

2.1 Frequency-Hopping Iterative Multi-Scaling Approach (IMSA-FH)

The first inversion algorithm is concerned with an integration of the $IMSA$ into a frequency hopping scheme. In such an integration the multi-frequency data ($p = 1, .., P$) are used in a cascade fashion starting from the lowest available frequency ($f = f_1$). At each stage of the hopping strategy ($p = 1, ..., P$), a nested multi-scaling procedure of S_p optimization steps processes the monochromatic data-set related to the p-th frequency. More in detail, the procedure can be summarized as follows

(a) *Frequency-Hopping Reconstruction Loop* ($p = 1, ..., P$)

($a.1$) *Initialization* ($s_p = 0$)

The investigation domain D_I is partitioned into N_p sub-domains according to the information content of the scattered field [8] at $f = f_p$ and, consequently, a suitable set of rectangular basis functions $[B_n(x,y),\ n = 1, ..., N_p]$ is defined. Moreover, the problem unknowns are initialized to the free-space configuration, by setting $E^{tot}_{v,p,s_p}(x,y)\Big|_{p=1,s_p=0} = E^{inc}_{v,p}(x,y)\Big|_{p=1}$ and $\tau_{p,s_p}(x,y)\Big|_{p=1,s_p=0} = \tau_0(x,y)$, when $p = 1$, otherwise the profile reconstructed at the convergence step of the $(p-1)$-th frequency stage is suitably mapped into the investigation domain [i.e., $E^{tot}_{v,p,s_p}(x,y)\Big|_{s_p=0} = E^{tot}_{v,p-1}(x,y)$ and $\tau_{p,s_p}(x,y)\Big|_{s_p=0} = \tau_{p-1}(x,y)$];

($a.2$) *Low-Order Reconstruction* ($s_p = 1$)

A homogeneous coarse reconstruction

$$\tau_{p,s_p}(x,y)\Big|_{s_p=1} = \sum_{n=1}^{N_1} \tau_{p,s_p}(x_n,\, y_n)\Big|_{s_p=1} B_n\,(x,\, y)\,, \quad (x,y) \in D_I \tag{4}$$

$$E^{tot}_{v,p,s_p}(x,y)\Big|_{s_p=1} = \sum_{n=1}^{N_1} E^{tot}_{v,p,s_p}(x_n,\, y_n)\Big|_{s_p=1} B_n\,(x,\, y)\,, \quad (x,y) \in D_I \tag{5}$$

is yielded by determining the set of unknown coefficients $\underline{f}_{p,s_p}\Big|_{s_p=1} = \Big\{ \tau_{p,s_p}(x_n,\, y_n)\Big|_{s_p=1}$, $E^{tot}_{v,p,s_p}(x_n,\, y_n)\Big|_{s_p=1}; n = 1, ..., N_p, v = 1, ..., V\}$, through the minimization of the low-order cost function

$$\Psi\left\{\underline{f}_{p,1}\right\} = \frac{\sum_{v=1}^{V} \sum_{m_{v,p}=1}^{M_{v,p}} \left| E^{scatt}_{v,p}\left(x_{m_{v,p}}, y_{m_{v,p}}\right) - S^{ext}_{v,p}\left\{\tau_{p,1}(x_n,y_n) E^{tot}_{v,p,1}(x_n,y_n)\right\}\right|^2}{\sum_{v=1}^{V} \sum_{m_{v,p}=1}^{M_{v,p}} \left| E^{scatt}_{v,p}\left(x_{m_{v,p}}, y_{m_{v,p}}\right)\right|^2} + \frac{\sum_{v=1}^{V} \sum_{n=1}^{N_p} \left| E^{inc}_{v,p}(x_n,y_n) - E^{tot}_{v,p,1}(x_n,y_n) + S^{int}_{v,p}\left\{\tau_{p,1}(x_n,y_n) E^{tot}_{v,p,1}(x_n,y_n)\right\}\right|^2}{\sum_{v=1}^{V} \sum_{n=1}^{N_p} \left| E^{inc}_{v,p}(x_n,y_n)\right|^2} \tag{6}$$

(a.3) Multi-Scaling Process $(s_p = 2, ..., S_p)$

(a.3.I) Multi-Scaling Profile Reconstruction

Starting from the solution $\underline{f}_{p,s_p-1}$ computed at the previous step $(s_p - 1)$, a set of Q^{s_p} regions-of-interest (*RoI*s), $D^{(q)}_{O(s_p-1)}$, is defined according to the *clustering procedure* described in [12] where the resolution level is increased $[R_{s_p} \leftarrow R_{s_p} + 1]$. Therefore a multi-resolution representation of the unknowns

$$\begin{gathered} \tau_{p,s_p}(x,y) = \sum_{r_{s_p}=1}^{R_{sp}} \sum_{n\left(r_{s_p}\right)=1}^{N\left(r_{s_p}\right)} \tau_{p,s_p}\left(x_{n\left(r_{s_p}\right)},\, y_{n\left(r_{s_p}\right)}\right) B_{n\left(r_{s_p}\right)}\,(x,\, y) \\ (x,y) \in D_I \\ E^{tot}_{v,p,s_p}(x,y) = \sum_{r_{s_p}=1}^{R_{sp}} \sum_{n\left(r_{s_p}\right)=1}^{N\left(r_{s_p}\right)} E^{tot}_{v,p,s_p}\left(x_{n\left(r_{s_p}\right)},\, y_{n\left(r_{s_p}\right)}\right) B_{n\left(r_{s_p}\right)}\,(x,\, y) \end{gathered} \tag{7}$$

r_{s_p} being the resolution index at the s_p-th step ranging from the largest characteristic length scale $(r_{s_p} = 1)$ up to the smallest basis-function support $(r_{s_p} = R_{s_p} = s_p)$, is looked for as the minimum of the multi-resolution cost function

$$\Psi\left\{\underline{f}_{p,s_p}\right\}=\frac{\sum_{v=1}^{V}\sum_{m_{v,p}=1}^{M_{v,p}}\left|E_{v,p}^{scatt}\left(x_{m_{v,p}},y_{m_{v,p}}\right)-S_{v,p}^{ext}\left\{\tau_{p,s_p}\left(x_{n\left(r_{s_p}\right)},y_{n\left(r_{s_p}\right)}\right)E_{v,p,s_p}^{tot}\left(x_{n\left(r_{s_p}\right)},y_{n\left(r_{s_p}\right)}\right)\right\}\right|^2}{\sum_{v=1}^{V}\sum_{m_{v,p}=1}^{M_{v,p}}\left|E_{v,p}^{scatt}\left(x_{m_{v,p}},y_{m_{v,p}}\right)\right|^2}+$$

$$\frac{1}{\sum_{v=1}^{V}\sum_{r_{s_p}=1}^{R_{s_p}}\sum_{n\left(r_{s_p}\right)=1}^{N\left(r_{s_p}\right)}\left|E_{v,p}^{inc}\left(x_{n\left(r_{s_p}\right)},y_{n\left(r_{s_p}\right)}\right)\right|^2}\sum_{v=1}^{V}\sum_{r_{s_p}=1}^{R_{s_p}}\sum_{n\left(r_{s_p}\right)=1}^{N\left(r_{s_p}\right)}\left\{w\left(x_{n\left(r_{s_p}\right)},\,y_{n\left(r_{s_p}\right)}\right)\right.$$

$$\left|E_{v,p}^{inc}\left(x_{n\left(r_{s_p}\right)},\,y_{n\left(r_{s_p}\right)}\right)-E_{v,p,s_p}^{tot}\left(x_{n\left(r_{s_p}\right)},\,y_{n\left(r_{s_p}\right)}\right)+\right.$$

$$\left.\left.S_{v,p}^{int}\left\{\tau_{p,s_p}\left(x_{n\left(r_{s_p}\right)},\,y_{n\left(r_{s_p}\right)}\right)E_{v,p,s_p}^{tot}\left(x_{n\left(r_{s_p}\right)},\,y_{n\left(r_{s_p}\right)}\right)\right\}\right|^2\right\} \tag{8}$$

where

$$w\left(x_{n\left(r_{s_p}\right)},\,y_{n\left(r_{s_p}\right)}\right)=\begin{cases}0\ if\ \left(x_{n\left(r_{s_p}\right)},\,y_{n\left(r_{s_p}\right)}\right)\notin D_{O(s_p-1)}^{(q)}\\ 1\ if\ \left(x_{n\left(r_{s_p}\right)},\,y_{n\left(r_{s_p}\right)}\right)\in D_{O(s_p-1)}^{(q)}\end{cases}\qquad q=1,...,Q^{s_p}$$

(a.3.II) Multi-Scaling Termination

The multi-scale process is stopped ($s_p = S_p^{opt} < S_p$) when a set of stability criteria on the reconstruction [11] hold true and the reached solution, $\underline{f}_{p,S_p^{opt}}$ is assumed as the estimated solution at the p-th frequency stage [i.e., $\tau_p(x,y)=\tau_{p,S_p^{opt}}(x,y)$ and $E_{v,p}^{tot}(x,y)=E_{v,p,S_p^{opt}}^{tot}(x,y)$]. Moreover, if $p=P$ then the loop over the frequencies ($f=f_1,...,f_P$) is terminated and the final dielectric profile returned, $\tau^{opt}(x,y)=\tau_p(x,y)$, as well as the field distributions $E_{v,p}^{opt}(x,y)=E_{v,p}^{tot}(x,y)$, $p=1,...,P$.

2.2 Multi-Frequency Iterative Multi-Scaling Approach (IMSA-MF)

Unlike the $IMSA-FH$, the $IMSA-MF$ represents a generalization of the $IMSA$ processing proposed in [11] for the reconstruction of single scatterers and extended in [12] for multiple-objects from single-frequency data. Accordingly, some assumptions on the scattering function (1) and a different data processing are needed. In the following, the distinctive issues of such an method will be briefly resumed.

(a) Multiple-Frequency Contrast Function Model

In order to avoid increasing the number of unknowns, hence compromising the benefits of dealing with multi-frequency data, the maxwellian model for the dispersion relationship is assumed

$$\tau_p(x,y) = Re\left[\tau_{ref}(x,y)\right] + j\frac{f_{ref}}{f_p} Im\left[\tau_{ref}(x,y)\right] \tag{9}$$

where the value of the contrast at the p-th frequency, $\tau_p(x,y)$, is related to that of the reference frequency f_{ref}, $\tau_{ref}(x,y)$. Therefore, the inversion process aimed at determining the unknown reference contrast function, $\tau_{ref}(x,y)$, instead of P distributions, thus profitably exploiting the multi-frequency data space and limiting the growing of the number of unknowns (with respect to the mono-frequency case) to the internal fields, $E^{tot}_{v,p}(x,y)$, $p = 1, ..., P$, that have to be estimated for each working frequency ($p = 1, .., P$) of the illumination setup;

(b) *Multi-Frequency Reconstruction Loop* ($s = 1, ..., S$)

Likewise the standard $IMSA$, a multi-scaling procedure of S ($s = 1, ..., S$) steps is performed in order to define the multi-resolution expansion of the unknown parameters

$$\begin{aligned} \tau_{ref}(x,y) &= \textstyle\sum_{r_s=1}^{R_s} \sum_{n(r_s)=1}^{N(r_s)} \tau_{ref}\left(x_{n(r_s)},\, y_{n(r_s)}\right) B_{n(r_s)}\left(x,\, y\right) \\ &\qquad (x,y) \in D_I \\ E^{tot}_{v,p}(x,y) &= \textstyle\sum_{r_s=1}^{R_s} \sum_{n(r_s)=1}^{N(r_s)} E^{tot}_{v,p}\left(x_{n(r_s)},\, y_{n(r_s)}\right) B_{n(r_s)}\left(x,\, y\right) \end{aligned} \tag{10}$$

being $N(R_s) = max_p\{N_p\}$ and $R_s = s$, by minimizing at each step of the reconstruction loop the *Multiple-Frequency Multi-Resolution Cost Function* defined as follows

$$\begin{aligned} \Psi\left\{\underline{f}_s\right\} = & \frac{\sum_{p=1}^{P}\sum_{v=1}^{V}\sum_{m_{v,p}=1}^{M_{v,p}}\left|E^{scatt}_{v,p}\left(x_{m_{v,p}},y_{m_{v,p}}\right) - S^{ext}_{v,p}\left\{\tau_{ref,s}\left(x_{n(r_s)},y_{n(r_s)}\right)E^{tot}_{v,p,s}\left(x_{n(r_s)},y_{n(r_s)}\right)\right\}\right|^2}{\sum_{p=1}^{P}\sum_{v=1}^{V}\sum_{m_{v,p}=1}^{M_{v,p}}\left|E^{scatt}_{v,p}\left(x_{m_{v,p}},y_{m_{v,p}}\right)\right|^2} + \\ & \frac{1}{\sum_{p=1}^{P}\sum_{v=1}^{V}\sum_{r_s=1}^{R_s}\sum_{n(r_s)=1}^{N(r_s)}\left|E^{inc}_{v,p}\left(x_{n(r_s)},y_{n(r_s)}\right)\right|^2} \sum_{v=1}^{V}\sum_{r_s=1}^{R_s}\sum_{n(r_s)=1}^{N(r_s)}\left\{w\left(x_{n(r_s)},\, y_{n(r_s)}\right)\right. \\ & \left|E^{inc}_{v,p}\left(x_{n(r_s)},\, y_{n(r_s)}\right) - E^{tot}_{v,p,s}\left(x_{n(r_s)},\, y_{n(r_s)}\right) + \right. \\ & \left.\left. S^{int}_{v,p}\left\{\tau_{ref,s}\left(x_{n(r_s)},\, y_{n(r_s)}\right) E^{tot}_{v,p,s}\left(x_{n(r_s)},\, y_{n(r_s)}\right)\right\}\right|^2\right\} \end{aligned} \tag{11}$$

where the unknown array turns out to be $\underline{f}_s = \left\{\tau_{ref}\left(x_{n(r_s)},\, y_{n(r_s)}\right),\, E^{tot}_{v,p,s}\left(x_{n(r_s)},\, y_{n(r_s)}\right)\right.$;

$n\,(r_s) = 1, ..., N\,(r_s),\ r_s = 1, ..., R_s,\ p = 1, ..., P,\ v = 1, ..., V\,\}$.

3 Numerical Analysis

In this Section, a selected set of representative inversion results are presented and discussed. The aim is to assess the reconstruction capabilities of the proposed multi-resolution strategies ($IMSA - MF$ and $IMSA - FH$) in comparison with the standard $IMSA$ [referred in the following as *Single-Frequency IMSA* ($IMSA - SF$)] and with respect to traditional single-step methods. As far as two-dimensional configurations are concerned, both synthetic and experimental data are presented and the limitations in reconstructing lossy structures are discussed. Moreover, as a representative example, the reconstruction of a three-dimensional layered structures is reported, as well.

3.1 Two-Dimensional Configurations

3.1.1 Numerical Testing - Layered Dielectric Profile

The geometry of the first test case is shown in Fig. $2(a)$. A layered cylinder lies at $x_c^{ref} = -y_c^{ref} = -0.6\,\lambda$ (λ being the wavelength at $f = 6\,GHz$) in a square investigation domain $L_{DI} = 3.0\,\lambda$- sided. The object function of the inner square layer ($L_{in} = 0.6\,\lambda$ in side) is $\tau_{in} = 0.5$, while that of the outer layer ($L_{out} = 0.9\,\lambda$-sided) is equal to $\tau_{out} = 2.0$. The investigation domain has been illuminated by a set of incident plane waves impinging from $V = 8$ equally-spaced directions. For each illumination, multi-frequency data [(1)] ($P = 3$, $f_1 = 5\,GHz$, $f_2 = 6\,GHz$, $f_3 = 7\,GHz$) have been simulated in a set of measurement points located on a circle $r_{D_O} = 3\,\lambda$ in radius. Because of the different information content available at each frequency [4][8], $M_{v,1} = 31$, $M_{v,2} = 37$ and $M_{v,3} = 44$ field samples have been taken into account at f_1, f_2 and f_3, respectively. Therefore, $N_1 = 121$, $N_2 = 144$, and $N_3 = 169$ basis functions have been used for the lower-order reconstruction ($IMSA - FH$ and $IMSA - SF$), while $N(R_s) = N_3$, $s = 1, ..., S$, has been chosen for the $IMSA - MF$ inversion.

In the framework of the comparative study, the results of the inversion process both for the

[(1)] The data have been blurred adding a Gaussian noise characterized by $SNR = 20dB$.

$IMSA-SF$ simulations [Figs. 2(b)-(d)] and for the $IMSA-MF$ approach [Fig. 2(e)] are shown in Fig. 2. As expected, the gray-level images of the object function pictorially point out that the reconstruction benefits of non-negligible improvements when multi-frequency data are exploited both in refining the outer and the inner layer. Such a qualitative impression is confirmed by the corresponding values of the error figures reported in Tab. I and defined as in [11]. Whatever the frequency used for the $IMSA-SF$ inversion, the $IMSA-MF$ turns out to be better guaranteeing enhanced performances. In particular $min_{p=1,2,3}\left\{\chi_{tot}^{IMSA-SF_p}\right\} \geq 2.21\chi_{tot}^{IMSA-MF}$, $min_{p=1,2,3}\left\{\chi_{int}^{IMSA-SF_p}\right\} \geq 1.20\chi_{int}^{IMSA-MF}$ and $min_{p=1,2,3}\left\{\chi_{ext}^{IMSA-SF_p}\right\} \geq 1.58\chi_{ext}^{IMSA-MF}$. Successively, in order to generalize these indications, the whole set of simulations in the frequency range between $3\,GHz$ and $7\,GHz$ has been performed. The results are resumed in Fig. 3 in terms of the total reconstruction error versus frequency [or the reference frequency f_{ref} for the $IMSA-MF$ when the $P=3$ adjacent frequencies ($f_{p-1}=f_{ref}-1\,GHz$, $f_p=f_{ref}$, $f_{p+1}=f_{ref}+1\,GHz$) are simultaneously processed]. As it can be observed, the accuracy of the multi-frequency strategy is on average of about $\triangle\chi_{tot}^{IMSA-SF/IMSA-MF}=40\%$ (being $\triangle\chi_{tot}^{i/j}=\frac{\chi_{tot}^{i}-\chi_{tot}^{j}}{\chi_{tot}^{i}}$) better than that of single-frequency multi-resolution methods.

For completeness, the $IMSA-MF$ has been compared to the other multi-resolution/multi-frequency approach ($IMSA-FH$). Moreover, as a reference, the inversion has been performed with single-step conjugate gradient-based strategies (also referred as "*bare*" approaches since a homogeneous discretization, according to the Richmond's criterion [15], of the D_I has been adopted) both in their frequency hopping ($CG-FH$) and multi-frequency ($CG-MF$) implementations. In Fig. 4(a) the dielectric profile retrieved with the $IMSA-FH$ strategy is shown. As it can be noticed (and confirmed by the error values given in Tab. I), the $IMSA$ slightly takes advantage of the frequency hopping scheme [carried out by considering the $P=3$ different frequencies used for the monochromatic simulations whose results are presented in Figs. 2(b)-(d)]. As a matter of fact, it turns out that $min_p\left\{\triangle\chi_{tot}^{IMSA-SF_p/IMSA-HF}\right\}=8.7\%$ and $max_p\left\{\triangle\chi_{tot}^{IMSA-SF_p/IMSA-HF}\right\}=34\%$ versus $min_p\left\{\triangle\chi_{tot}^{IMSA-SF_p/IMSA-MF}\right\}=54\%$ and $max_p\left\{\triangle\chi_{tot}^{IMSA-SF_p/IMSA-MF}\right\}=67\%$.

On the other hand, it should be noticed that multi-resolution strategies ($IMSA-MF$ and $IMSA-FH$) allow a non-negligible improvement of the reconstruction effectiveness

in comparison with the corresponding "bare" approaches [$CG-MF$ - Fig. 4(b) and $CG-HF$ - Fig. 4(c)] since $\triangle\chi_{tot}^{CG-FH/IMSA-FH} = 36\%$ and $\triangle\chi_{tot}^{CG-MF/IMSA-MF} = 55\%$. As far as the computational issues are concerned, a general overview is given in Tab. II where a set of representative parameters are reported. In particular, the number of unknowns (U), the total number of conjugate-gradient iterations needed for reaching the convergence solution (K_{tot}), the mean time per iteration (t_k), and the global CPU time (T_{tot}) are given. Unavoidably, because of the larger dimension of the set of scattering data, the simultaneous multi-frequency processing requires greater storage resources ($U^{IMSA-MF} = 8500$ and $U^{CG-MF} = 18052$ vs. $U^{IMSA-SF} = U^{IMSA-FH} = 3042$ and $U^{CG-FH} = 6515$) and an increasing of the computational burden for each iteration ($t_k^{IMSA-MF} = 4.5\,sec$ and $t_k^{CG-MF} = 20.2\,sec$ vs. $t_k^{IMSA-SF} = t_k^{IMSA-FH} = 0.5\,sec$ and $t_k^{CG-FH} = 1.32\,sec$). On the other hand, as expected and also demonstrated in the monochromatic case, the multi-resolution technique limit the computational costs both in terms of unknowns ($U^{IMSA-MF} \simeq 2.12\,U^{CG-MF}$ and $U^{IMSA-FH} \simeq 2.14\,U^{CG-FH}$) and CPU time ($t_k^{CG-MF} \simeq 4.5\,t_k^{IMSA-MF}$ and $t_k^{CG-FH} \simeq 2.64\,t_k^{IMSA-FH}$).

3.1.2 Numerical Testing - Lossy Profile

The second test case deals with a lossy profile. A square cylindrical structure, whose dimensions are those of the inner layer used of the previous experiments, and characterized by an object function $\tau = 0.5 - j\frac{\sigma}{2\pi f_p \varepsilon_o}$ has been considered. For a sensitivity study, σ has been varied in the range $0.0\,\frac{S}{m} \leq \sigma \leq 1.0\,\frac{S}{m}$.

The experiments carried out through the $IMSA-MF$ indicate that the object under test is quite faithfully retrieved, even though there is an increasing of the values of the reconstruction errors [χ_{tot}^{re} - Fig. 5(a); χ_{tot}^{im} - Fig. 5(b)] when the conductivity grows. Moreover, the comparisons with other $IMSA$-based approaches shows that the $IMSA-MF$ scheme usually improves the effectiveness of the retrieval procedure and the accuracy in reconstructing the imaginary part is lower [Fig. 5(b)] than that in dealing with the real part [Fig. 5(a)], especially when the FH scheme is exploited. Therefore, the latter does not seem the most effective methodology for obtaining a good estimation of the conductivity distribution. Eventually, one can also observe that the values of the internal

[χ_{int}^{im} - Fig. 5(d)] and total [χ_{tot}^{im} - Fig. 5(b)] errors present a peak below $\sigma = 0.1\,\frac{S}{m}$. This is due to the difficulty of an accurate reconstruction of the imaginary part when its value is much lower than that of the real part.

Successively, a layered configuration for both the permittivity and conductivity profiles has been taken into account. In particular, the real part of the contrast is distributed as in the test case of Fig. 2(a), while the imaginary part is shown in Fig. 6(a), where the inner layer is characterized by $\sigma_{in} = 0.5\,\frac{S}{m}$ and the outer one by $\sigma_{out} = 0.1\,\frac{S}{m}$. Such a reference profile has been reconstructed with the $IMSA - MF$ and the results reported in Figs. 6(b)(c). As it can be noticed, the layered distribution has been satisfactorily imaged. Moreover, in order to give a wider overview on potentialities and current limitations of the proposed strategies, the behaviors of the error figures when varying σ_{in} and σ_{out} from $0.0\,\frac{S}{m}$ up to $0.5\,\frac{S}{m}$ are shown in Fig. 7. As expected, they confirm that the accuracy in estimating the conductivity distribution is lower than that in retrieving than the permittivity profile. As a matter of fact, $\chi_{tot}^{re} < 3.8\%$ while $\chi_{tot}^{im} < 11\%$.

3.1.3 Experimental Testing - Multiple Scatterers

In order to further assess the indications drawn from the synthetic testing, an experimental validation has been then performed. The scattering data are kindly available from the *Institute Fresnel* in Marseille (France) and the configuration of the measurement set-up has been carefully described in [16]. The measurements have been collected in the frequency range from $2\,GHz$ and $10\,GHz$ at $M_{v,p} = 241$ positions for each of the $V = 18$ illuminations. As a representative benchmark, the TM-polarized data concerned with the so-called "*FoamDielExtTM*" geometry [Fig. 8(a)] have been processed. In such a test case, the scatterer under test is composed by two cylinders characterized by object functions: $\tau_1 = 0.45$ and $\tau_2 = 2.0$. Moreover, the two-dimensional assumption can be made since the scatterers are long with respect to the wavelength in the z-direction.

As far as the comparative study is concerned, let us consider as a reference result that obtained processing monochromatic data ($f = 5\,GHz$) with the $IMSA - SF$ [Fig. 8(b)] and by considering an initial discretization grid of $N = 256$ sub-domains (more results at different frequencies are presented in [17]). Concerning the $IMSA - MF$, the inversion

[Fig. $8(c)$] has been carried out by using $P = 4$ frequencies in the range between $f_{min} = 2\,GHz$ and $f_{max} = 5\,GHz$ with a frequency step of $\triangle f = 1\,GHz$. Moreover, the analysis has been completed with the reconstructions by means of the $IMSA - FH$ [Fig. $9(a)$], the $CG - MF$ [Fig. $9(b)$], and the $CG - FH$ [Fig. $9(c)$]. It is worth noting that the investigation domain D_I for the "bare" approaches has been partitioned into $N = 400$ sub-domains in order to reach a satisfactory spatial resolution in the estimated profile.

From a qualitative point of view, the gray-level plots confirm that usually the use of multi-frequency data improves the accuracy of the reconstructions. More in detail, the reconstructed profiles better reproduce the actual distribution especially concerning the homogeneity of the scatterers except for the $IMSA - FH$. In such a case, the hopping strategy turns out to be effective in defining the structure and the contrast value of the stronger scatterer, while some problems occur in shaping the weaker object. On the other hand, it should be noticed that single step algorithms [Fig. $9(b)$ e Fig. $9(c)$] underestimate the value of object function inside the support of the smaller scatterer ($\tau_2^{CG-MF} \simeq \tau_2^{CG-FH} \simeq 1.5$) and they require more computational resources than $IMSA$-based procedures as pointed out in the previous sub-section.

3.2 Three-Dimensional Configuration

This section presents some representative results and considerations on the reconstruction of three-dimensional multilayer structures from multi-frequency data. In such a case, the investigation domain is a cube $L_{ind} = 1.2\,\lambda$-sided and it has been illuminated by $V = 4$ plane waves impinging from $\theta_{inc} = \pi/2$, $\phi_{inc} = \frac{(v-1)\pi}{2}$ clockwise with respect to the z axis. A set of points-like receivers ($M_{v,p} = 21$) has been located in $G = 3$ rings ($\rho_{m,v,p} = 2.93\lambda$ in radius) at the positions $\phi_{m,v,p}^{scatt} = \phi_{v,p}^{inc} + 2\pi G\frac{(m_{v,p}-1)}{M_{v,p}}$ and $z_{v,m} = \left[1 - G\frac{(m_{v,p}-1)}{M_{v,p}}\right] z_0$, $z_0 = 0.06\lambda$. Moreover, the collected data have been blurred by adding a Gaussian noise with $SNR = 30\,dB$.

In such an arrangement, a multilayer profile of volume $0.6\times0.6\times0.6\lambda^3$ has been positioned at ($x_b = y_b = z_b = 0.0$). The object function of the three layers is $\tau_1 = 0.5$, $\tau_2 = 1.0$ and $\tau_3 = 1.5$, respectively, and the volume of each layer is $0.2 \times 0.6 \times 0.6\lambda^3$. The reference distribution is shown in Fig. 10 [$z = 0.0$ plane in Fig. $10(a)$ and $x = 0.0$ plane in

Fig. 10(b)]. As far as the inverse problem is concerned, the investigation domain has been initially uniformly discretized into $N = 5 \times 5 \times 5$ cubic cells and a 3D frequency hopping scheme has been adopted ($P = 2$ - $f_1 = 1\,GHz$, $f_2 = 2\,GHz$). The retrieval obtained at the second hop ($s_2 = 2$) of the $IMSA - FH$ (Fig. 11) clearly points out the layered structure of the object under test. The use of the hopping scheme together with the multi-scaling approach improves the accuracy of the reconstruction procedure as indicated by the behaviors of the error figures in Tab. III.

On the other hand, it should be pointed out that certainly the simultaneous processing of multi-frequency data would allow a further improvement of the reconstruction accuracy, but this would unavoidably require additional computational resources. In order to limit the impact of such an issue in multi-frequency approaches, fast and efficient numerical methods are needed to be fully exploited through a multi-resolution allocation of the unknowns. A preliminary indication of such a possibility and of the arising advantages, let us consider the reconstruction of the previous scattering scenario when both the imaginary and the real part of the contrast function are unknown. By considering a "*bare*" single frequency approach ($CG - SF$), $U^{GC-SF} = 3250$ are the unknowns parameters and the mean time per iteration is of about $t_k^{CG-SF} \simeq 5.80\,s$. Dealing with a multi-frequency implementation, the dimension of the unknowns space becomes $U^{GC-MF} = 25600$ and $t_k^{CG-MF} \simeq 45.64\,s$[(2)]. On the contrary, an exploitation of the proposed $IMSA - MF$ strategy would require a mean time per iteration of $t_k^{IMSA-MF} \simeq 11.14\,s$ for reconstructing $U^{IMSA-MF} = 6250$ parameters (such a configuration provides a resolution level of the same order of the $CG - MF$) without leading to an increasing of the computational costs (with respect to the standard single-step approach), thanks to the adaptive allocation at each step of the unknowns.

4 Conclusions

In this paper, starting from a set of representative test cases, a comparative assessment of two multi-resolution approaches exploiting multi-frequency data has been carried out. The objective was that of giving some indications on the most suitable strategy able to

[(2)] It has been supposed to discretize the investigation domain in $N = 8 \times 8 \times 8$ cubic cells.

improve in a non-negligible fashion the reconstruction accuracy with a reasonable amount of computational resources compared to that of single-step methodologies. As a matter of fact, unlike the $IMSA-FH$, the $IMSA-MF$ provided numerical proofs of the enhanced effectiveness in processing multi-frequency information. Moreover, the numerical and experimental analysis pointed out current limitations of the proposed approach in reconstructing lossy profiles and the computational needs of the three-dimensional multi-frequency multi-scaling procedure that, even though demanding, is considerably more effective than the single step procedure. On the other hand, although the $IMSA-MF$ demonstrated an acceptable robustness to the choice of illumination frequencies, the numerical and experimental analysis pointed out that great care should be exercised in determining the informative amount in multi-frequency scattering data and how (and in which quantity) to process different data-sets. As a matter of fact, such issues, currently under study, strongly affect the performance of each multi-resolution multi-frequency procedure since they play a key-role both in allowing a good trade-off between suitable resolution level in the reconstruction, occurrence of local minima, and ill-conditioning of the whole inversion.

Future developments of such a research work will be aimed at theoretically (without heuristic rules or expensive test-and-trial numerical investigations) quantifying the dimension of the scattering data space as well as the independent information content of each frequency data-set for a more effective exploitation of multi-frequency measurements through multi-resolution approaches.

References

[1] M. Benedetti, M. Donelli, G. Franceschini, M. Pastorino, and A. Massa, "Effective exploitation of the a priori information through a microwave imaging procedure based on the SMW for NDE/NDT applications," *IEEE Trans. Geosci. Remote Sensing*, vol. 43, pp. 2584-2592, Nov. 2005.

[2] P. M. Meaney, M. W. Fanning, D. Li, S. P. Poplack, and K. D. Paulsen, "A clinical prototype for active microwave imaging of the breast," *IEEE Trans. Microwave Theory Tech.*, vol. 48, pp. 1841-1851, Nov. 2000.

[3] D. J. Daniels, *Subsurface Penetrating Radar.* London, U. K.: IEE Press, 1996.

[4] O. M. Bucci and G. Franceschetti, "On the degrees of freedom of scattered fields," *IEEE Trans. Antennas Propagat.*, vol. 37, pp. 918-926, Jul. 1989.

[5] S. Caorsi, G. L. Gragnani, and M. Pastorino, "An approach to microwave imaging using a multiview moment method solution for a two-dimensional infinite cylinder," *IEEE Trans. Microwave Theory Tech.*, vol. 39, pp. 1062-1067, Jun. 1991.

[6] O. S. Haddadin and E. S. Ebbini, "Imaging strongly scattering media using a multiple frequency distorted Born iterative method," *IEEE Trans. Ultrason. Ferroelect. Freq. Contr.*, vol. 45, pp. 1485-1496, Nov. 1998.

[7] K. Belkebir, R. Kleinmann, and C. Pichot, "Microwave imaging - Location and shape reconstruction from multifrequency data," *IEEE Trans. Microwave Theory Tech.*, vol. 45, pp. 469-475, Apr. 1997.

[8] O. M. Bucci, L. Crocco, T. Isernia, and V. Pascazio, "Inverse scattering problems with multifrequency data: reconstruction capabilities and solution strategies," *IEEE Trans. Geosci. Remote Sensing*, vol. 38, pp. 1749-1756, Jul. 2000.

[9] A. G. Tijhuis, K. Belkebir, A. C. S. Litman, ans B. P. de Hon, "Theoretical and computational aspects of 2-D inverse profiling," *IEEE Trans. Geosci. Remote Sensing*, vol. 39, pp. 1316-1330, Jul. 2001.

[10] A. Baussard, "Inversion of multi-frequency experimental data using an adaptive multiscale approach", *Inverse Problems*, vol. 21, pp. S15-S31, Dec. 2005.

[11] S. Caorsi, M. Donelli, D. Franceschini, and A. Massa, "A new methodology based on an iterative multiscaling for microwave imaging," *IEEE Trans. Microwave Theory Tech.*, vol. 51, pp. 1162-1173, Apr. 2003.

[12] S. Caorsi, M. Donelli, and A. Massa, "Detection, location, and imaging of multiple scatterers by means of the iterative multiscaling method," *IEEE Trans. Microwave Theory Tech.,* vol. 52, pp. 1217-1228, Apr. 2004.

[13] E. L. Miller and A. S. Willsky, "A multiscale, statistically based inversion scheme for linearized inverse scattering problems," *IEEE Trans. Geosci. Remote Sensing*, vol. 34, pp. 346-357, Mar. 1996.

[14] O. M. Bucci, L. Crocco, and T. Isernia, "An adaptive wavelet-based approach for non destructive evaluation applications," in *Proc. IEEE Antennas Propagation Symp.*, vol. 3, pp. 1756-1759, 2000.

[15] J. H. Richmond, "Scattering by a dielectric cylinder of arbitrary cross section shape," *IEEE Trans. Antennas Propagat.*, vol. 13, pp. 334-341, May 1965.

[16] J.-M. Geffrin, P. Sabouroux, and C. Eyraud, "Free space experimental scattering database continuation: experimental set-up and measurement precision," *Inverse Problems*, vol. 21, pp. S117-S130, Dec. 2005.

[17] M. Donelli, D. Franceschini, A. Massa, M. Pastorino, and A. Zanetti, "Multiresolution iterative inversion of real inhomogeneous targets," *Inverse Problems*, vol. 21, pp. S51-S63, Nov. 2005.

Figure Caption

- **Figure 1.** Sketch of the two-dimensional imaging configuration.

- **Figure 2.** *Numerical Testing - Layered profile.* (a) Reference distribution of the object function. Reconstructed profiles ($SNR = 20dB$) by means of the $IMSA-SF$ at the working frequency of (b) $f = 5\,GHz$, (c) $f = 6\,GHz$ and (d) $f = 7\,GHz$. (e) Comparison with the results obtained by means of the $IMSA - MF$ ($f = 5, 6, 7\,GHz$).

- **Figure 3.** *Numerical Testing - Layered profile.* Behavior of the quantitative error figures versus the working frequency ($IMSA-SF$) and the reference frequency f_{ref} ($IMSA - MF$).

- **Figure 4.** *Numerical Testing - Layered profile.* Reconstructions obtained with (a) $IMSA - FH$, (b) $CG - MF$, and (c) $CG - FH$, respectively.

- **Figure 5.** *Homogeneous lossy profile.* Behavior of the error figures versus the conductivity. *(a)* χ^{re}_{tot}, *(b)* χ^{im}_{tot}, *(c)* χ^{re}_{int} and *(d)* χ^{im}_{int} .

- **Figure 6.** *Layered lossy profile.* (a) Imaginary part of the reference distribution of the object function. Reconstructed profile ($SNR = 20dB$) by means of the $IMSA - MF$ ($f = 5, 6, 7\,GHz$) [(b) real and (c) imaginary part] when $\sigma_{int} = 0.5\,S/m$ and $\sigma_{ext} = 0.1\,S/m$.

- **Figure 7.** *Layered lossy profile.* Behavior of *(a)* χ^{re}_{tot} and *(b)* χ^{im}_{tot} versus the conductivity.

- **Figure 8.** *Experimental Testing - 'FoamDielExtTM' Configuration.* (a) Sketch of the object under test. Reconstruction results obtained with (b) $IMSA - SF$ ($f = 5\,GHz$) and (c) $IMSA - MF$ ($f = 2, 3, 4, 5\,GHz$).

- **Figure 9.** *Experimental Testing - 'FoamDielExtTM' Configuration.* Reconstruction results obtained with (a) $IMSA-FH$, (b) $CG-MF$, and (c) $CG-FH$ processing the set of frequencies $f = 2, 3, 4, 5\,GHz$.

- **Figure 10.** *Multi-layer dielectric cube* - Actual profile: (a) $z-plane$ and (b) $x-plane$.

- **Figure 11.** *Multi-layer dielectric cube* - Reconstruction obtained at $s_2 = S_{opt} = 2$: (a) $z = 0.0\lambda$ plane and (b) $x = 0.0\lambda$ plane.

Table Caption

- **Table I.** *Numerical Testing - Layered profile.* Values of the quantitative error figures at the convergence.
- **Table II.** *Numerical Testing - Layered profile.* Values of the computational indexes.
- **Table III.** *Multi-layer dielectric cube* - Error figures vs steps at the different hops of the $IMSA - FH$.

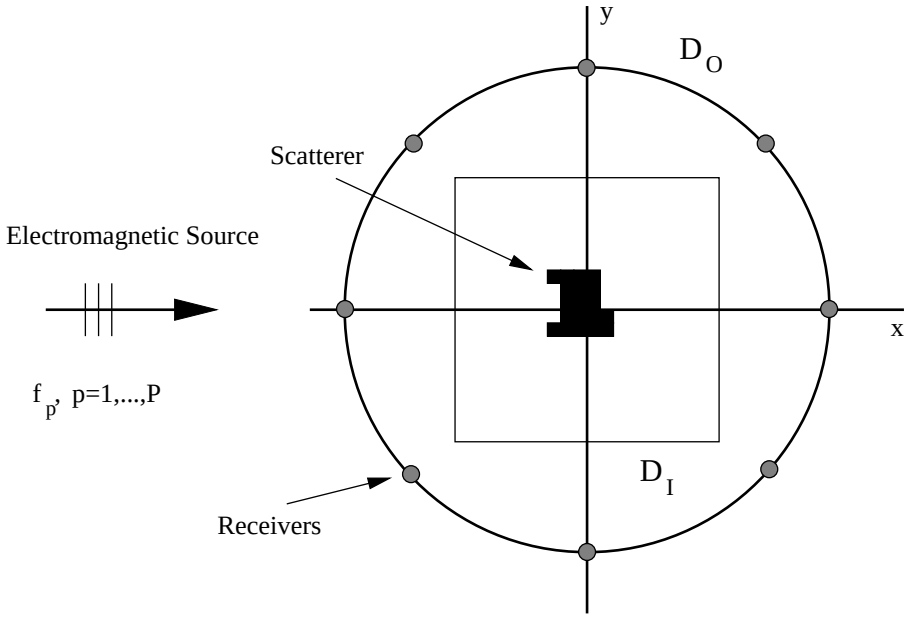

Figure 1 - D. Franceschini *et al.*, *"Dealing with Multi-Frequency Scattering Data.."*

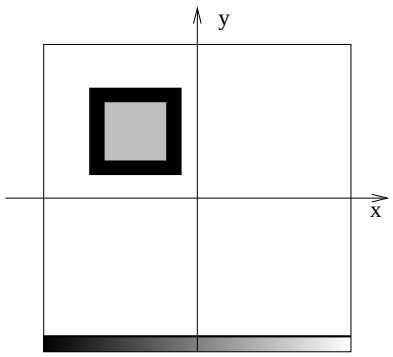

2.3 $Re\{\tau(x,y)\}$ 0.0

(a)

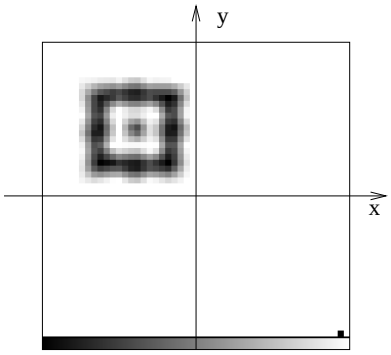

2.3 $Re\{\tau(x,y)\}$ 0.0

(b)

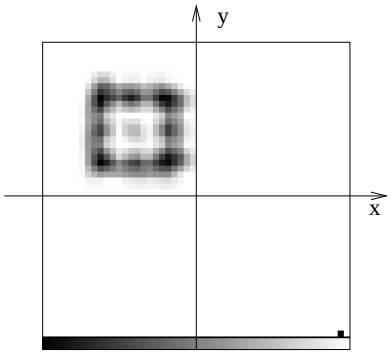

2.3 $Re\{\tau(x,y)\}$ 0.0

(c)

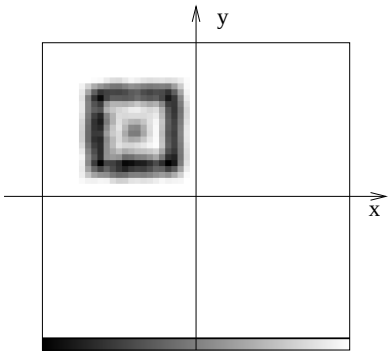

2.3 $Re\{\tau(x,y)\}$ 0.0

(d)

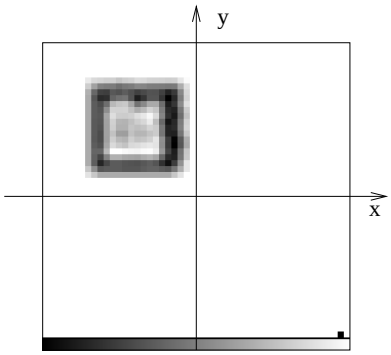

2.3 $Re\{\tau(x,y)\}$ 0.0

(e)

Figure 2 - D. Franceschini *et al.*, *"Dealing with Multi-Frequency Scattering Data..."*

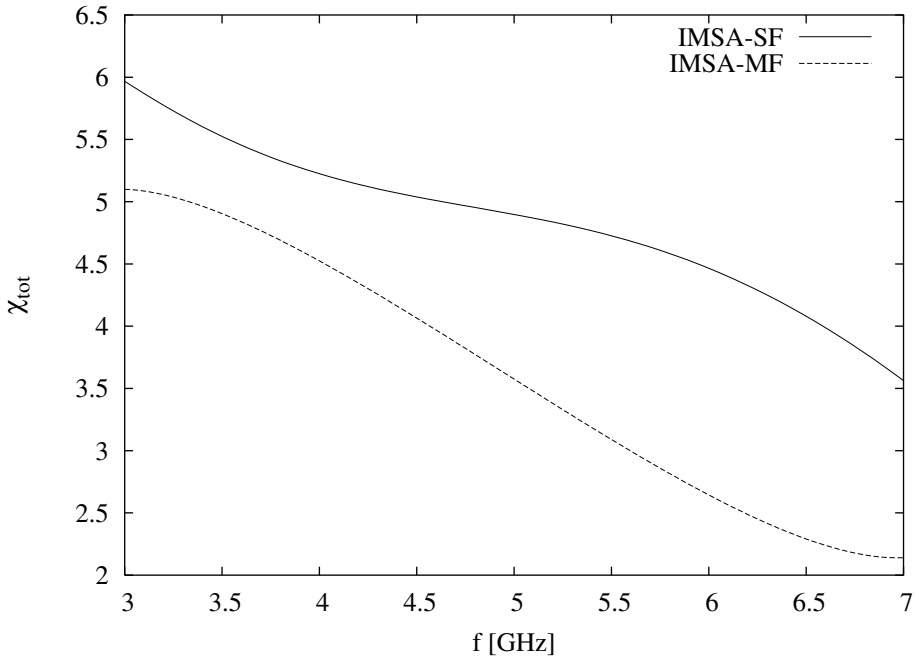

Figure 3 - D. Franceschini *et al.*, *"Dealing with Multi-Frequency Scattering Data..."*

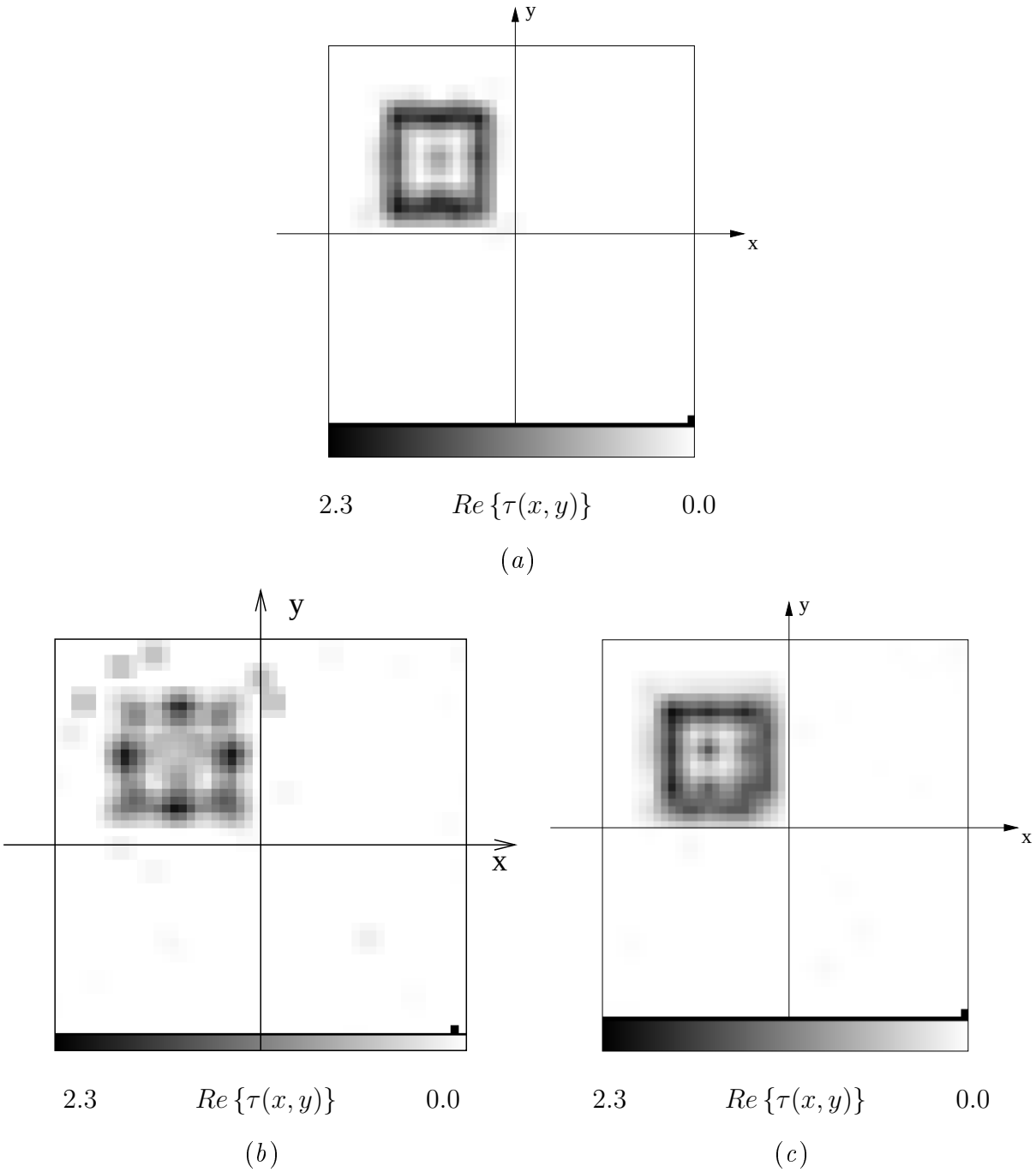

Figure 4 - D. Franceschini *et al.*, *"Dealing with Multi-Frequency Scattering Data..."*

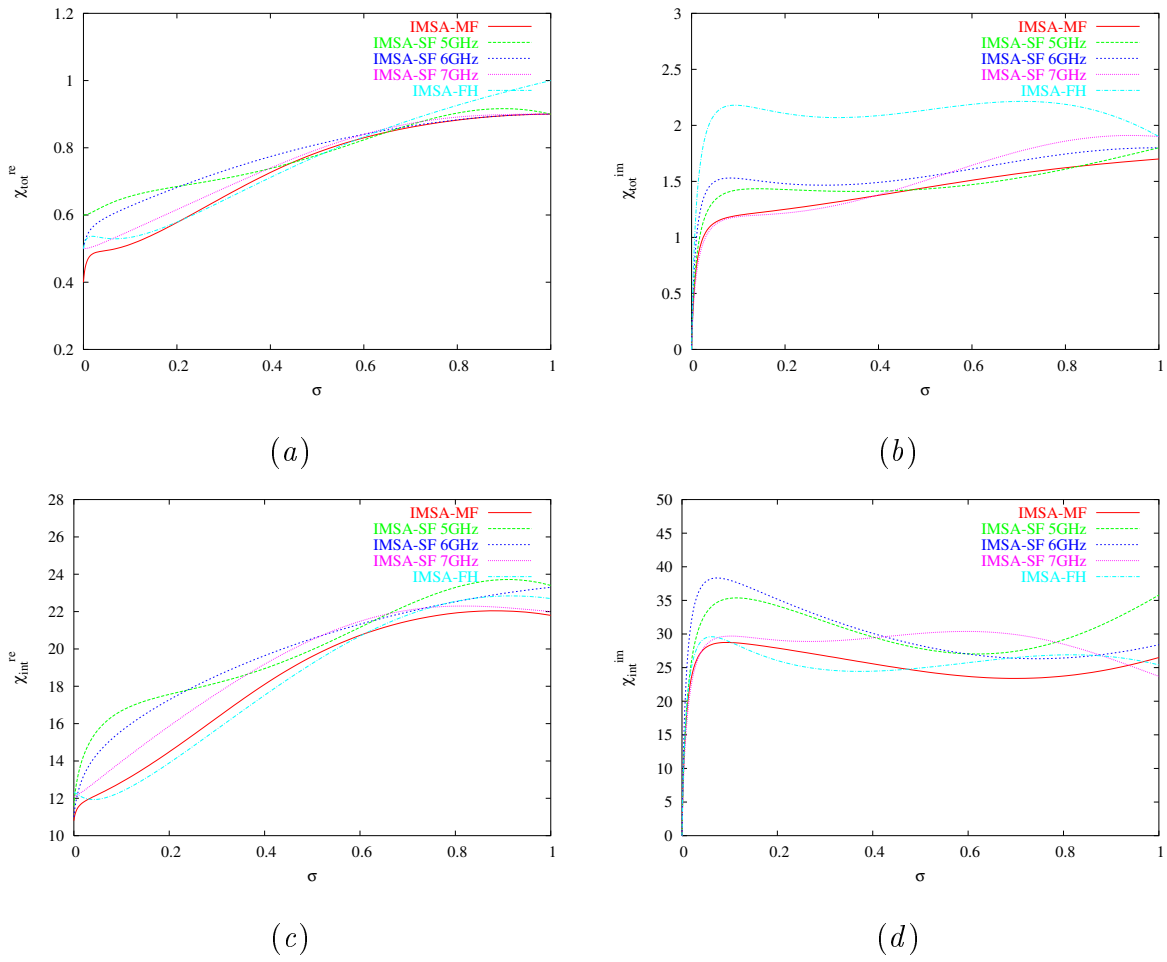

Figure 5 - D. Franceschini *et al.*, *"Dealing with Multi-Frequency Scattering Data..."*

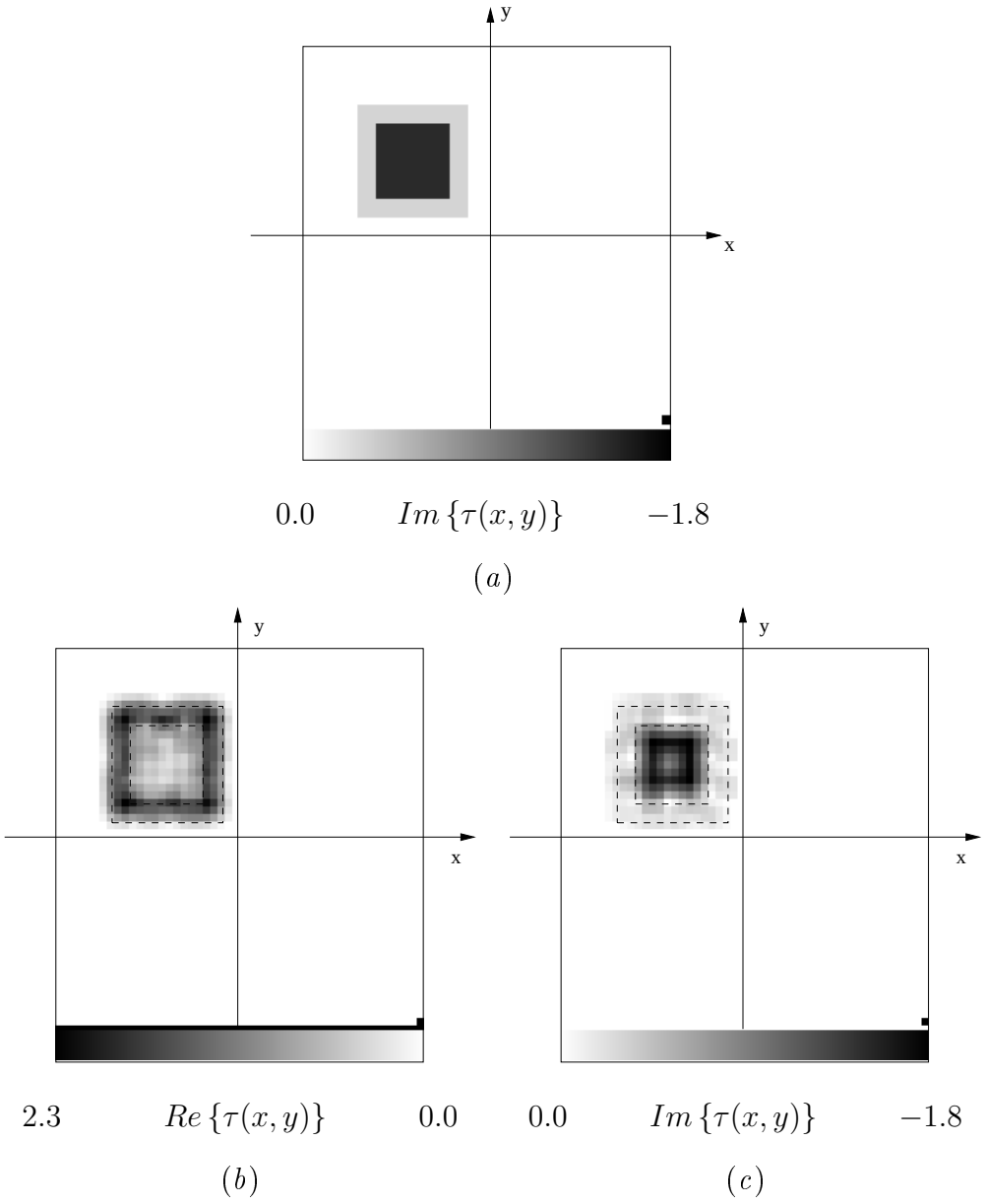

Figure 6 - D. Franceschini *et al.*, *"Dealing with Multi-Frequency Scattering Data..."*

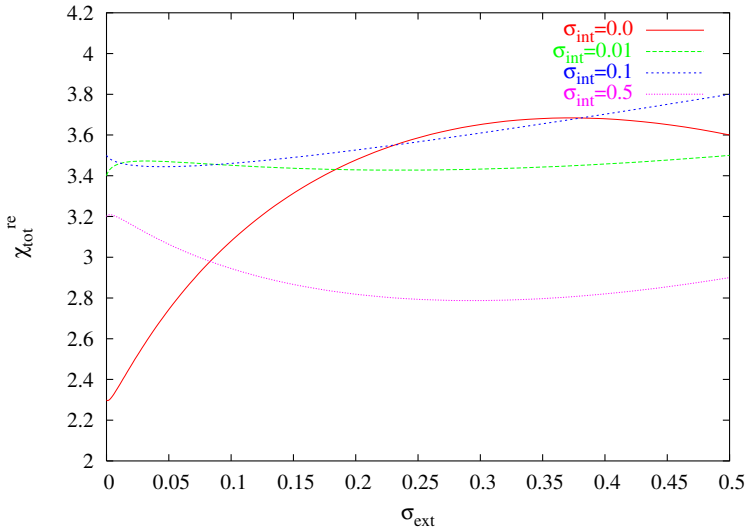

(a)

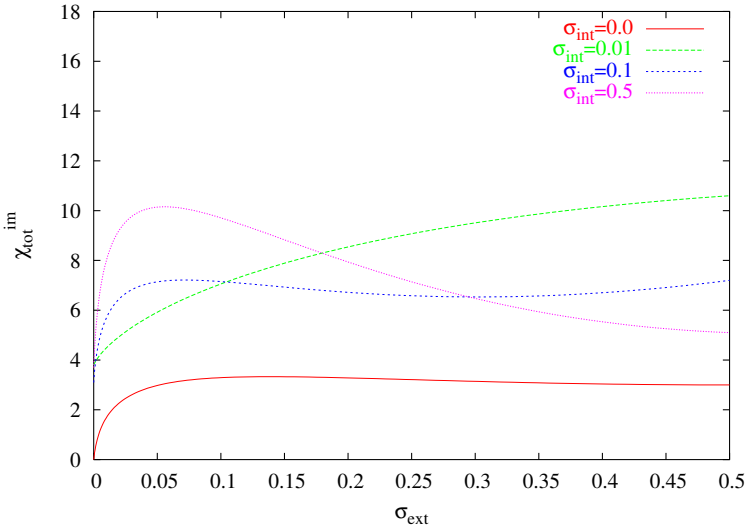

(b)

Figure 7 - D. Franceschini *et al.*, *"Dealing with Multi-Frequency Scattering Data..."*

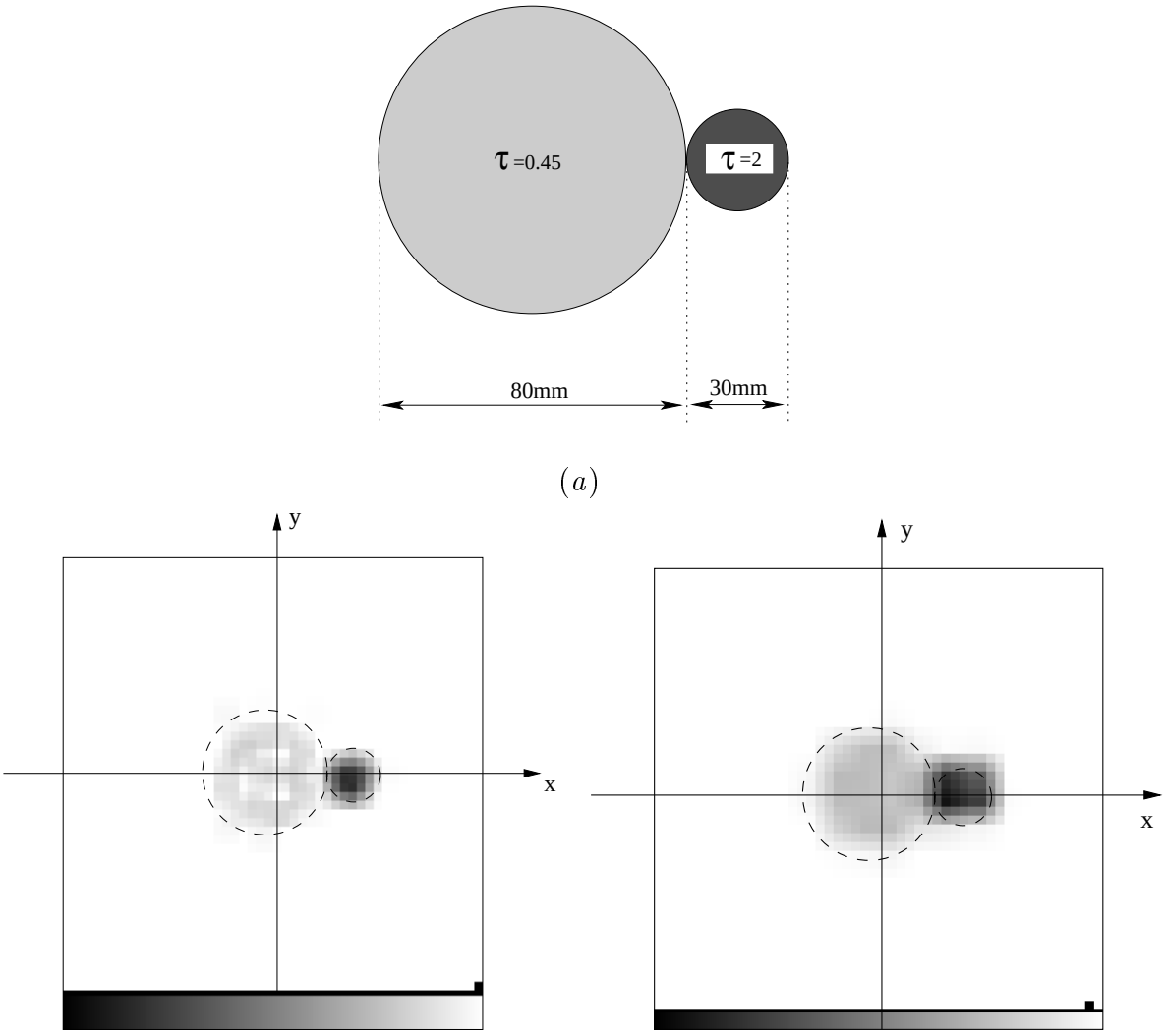

Figure 8 **- D. Franceschini *et al.***, *"Dealing with Multi-Frequency Scattering Data..."*

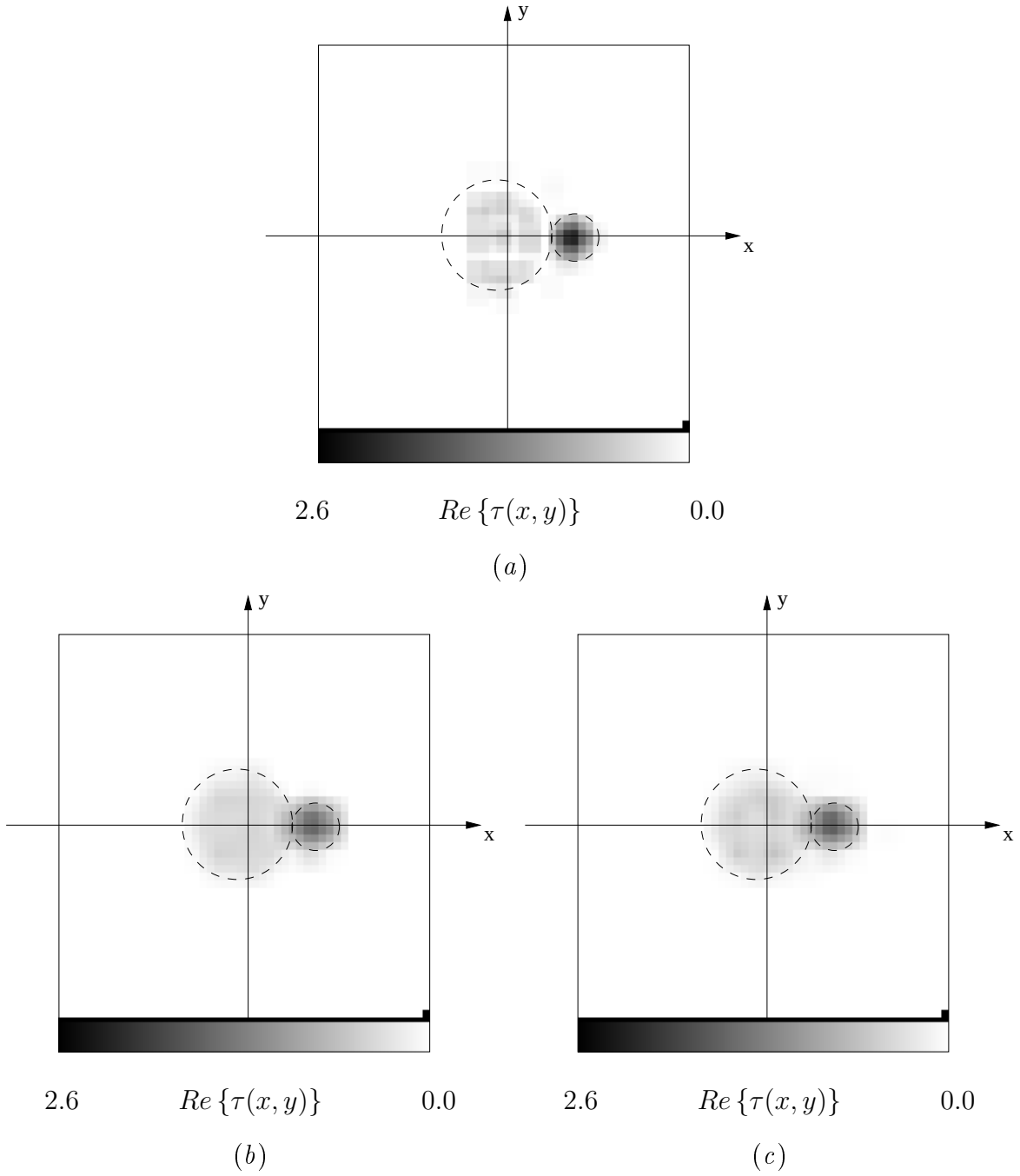

Figure 9 **- D. Franceschini *et al.*,** *"Dealing with Multi-Frequency Scattering Data..."*

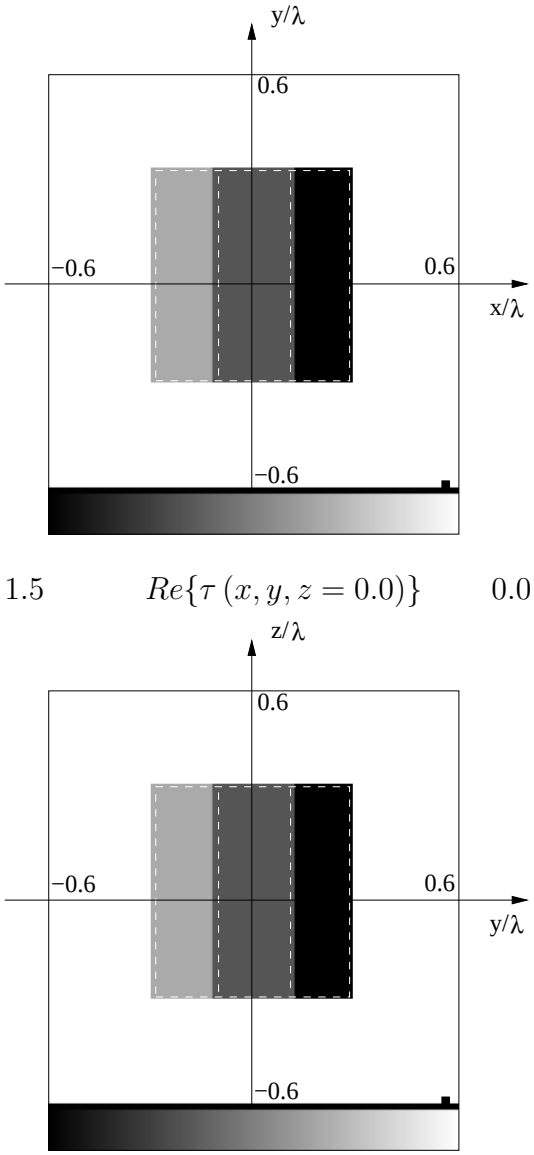

Figure 10 - D. Franceschini *et al.*, *"Dealing with Multi-Frequency Scattering Data..."*

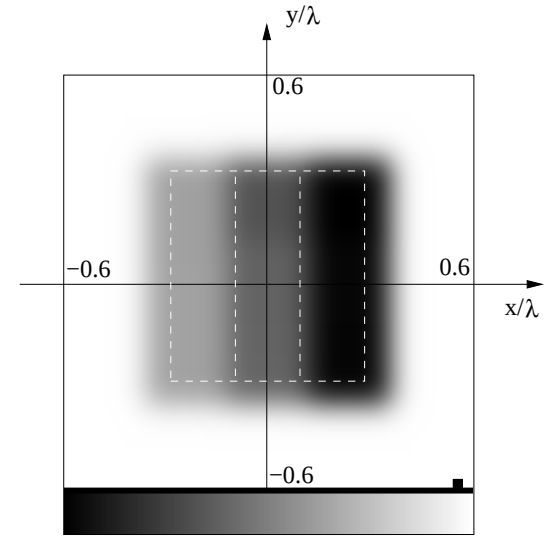

1.5 $Re\{\tau\,(x, y, z = 0.0)\}$ 0.0

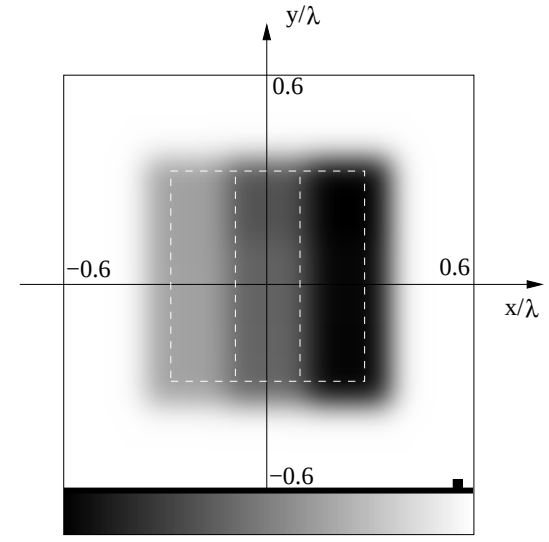

1.5 $Re\{\tau\,(x = 0.0, y, z)\}$ 0.0

Figure 11 - D. Franceschini *et al.*, *"Dealing with Multi-Frequency Scattering Data..."*

	χ_{tot}	χ_{int}	χ_{ext}
$IMSA-SF\ \ (f=5\,GHz)$	6.40	41.51	3.03
$IMSA-SF\ \ (f=6\,GHz)$	5.32	37.26	2.69
$IMSA-SF\ \ (f=7\,GHz)$	4.59	27.35	2.34
$IMSA-MF\ \ (f=5,6,7\,GHz)$	2.07	23.10	1.48
$IMSA-FH\ \ (f=5,6,7\,GHz)$	4.19	28.69	1.77
$CG-MF\ \ (f=5,6,7\,GHz)$	4.62	25.12	2.60
$CG-FH\ \ (f=5,6,7\,GHz)$	6.62	25.32	4.77

	U	K_{tot}	$t_k[s]$	$T_{tot}[s]$
$IMSA-SF\ \ (f=7GHz)$	3042	1820	0.5	0.8×10^3
$IMSA-MF\ \ (f=5,6,7GHz)$	8500	4553	4.5	20.5×10^3
$IMSA-FH\ \ (f=5,6,7GHz)$	3042	7287	0.5	3.4×10^3
$CG-MF\ \ (f=5,6,7GHz)$	18052	1356	20.2	27.4×10^3
$CG-FH\ \ (f=5,6,7GHz)$	6515	2180	1.32	2.9×10^3

p	s_p	χ_{tot}	χ_{int}	χ_{ext}
1	1	19.31	53.01	38.87
1	2	8.45	15.68	24.06
2	1	7.21	13.11	21.17
2	2	6.95	10.11	17.61

Table III - D. Franceschini *et al.*, *"Dealing with Multi-Frequency Scattering Data..."*